Phase diagram of the ultrafast photoinduced insulator-metal transition in vanadium dioxide

T. L. Cocker,[1,*] L. V. Titova,[1] S. Fourmaux,[2] G. Holloway,[1] H.-C. Bandulet,[2] D. Brassard,[2] J.-C. Kieffer,[2] M. A. El Khakani,[2] and F. A. Hegmann[1,†]

[1]*Department of Physics, University of Alberta, Edmonton, Alberta T6G 2E1, Canada*

[2]*INRS-EMT, Université du Québec, Varennes, Québec J3X 1S2, Canada*

(Received 4 December 2011; published 11 April 2012)

We use time-resolved terahertz spectroscopy to probe the ultrafast dynamics of the insulator-metal phase transition induced by femtosecond laser pulses in a nanogranular vanadium dioxide (VO_2) film. Based on the observed thresholds for characteristic transient terahertz dynamics, a phase diagram of critical pump fluence versus temperature for the insulator-metal phase transition in VO_2 is established for the first time over a broad range of temperatures down to 17 K. We find that both Mott and Peierls mechanisms are present in the insulating state and that the photoinduced transition is nonthermal. We propose a critical-threshold model for the ultrafast photoinduced transition based on a critical density of electrons and a critical density of coherently excited phonons necessary for the structural transition to the metallic state. As a result, evidence is found at low temperatures for an intermediate metallic state wherein the Mott state is melted but the Peierls distortion remains intact, consistent with recent theoretical predictions. Finally, the observed terahertz conductivity dynamics above the photoinduced transition threshold reveal nucleation and growth of metallic nanodomains over picosecond time scales.

DOI: 10.1103/PhysRevB.85.155120 PACS number(s): 63.20.kd, 64.60.Ht, 72.80.Ga, 78.47.D−

I. INTRODUCTION

Correlated electron materials can exhibit a diverse array of dramatic physical behavior, but understanding the origins of their emergent phenomena is hindered by the inherent difficulty of solving many-body problems. Vanadium dioxide (VO_2) has been intensely studied as a model system for metal-insulator transitions ever since its phase switching behavior near room temperature was discovered in 1959.[1] Simultaneous changes to both the electronic structure and crystal lattice have complicated the interpretation of the phase change, and a comprehensive description remains elusive. Competing theories have long attributed the effect to exclusively either a Peierls instability[2–4] or a Mott transition[5,6] citing electron-phonon or electron-electron interactions as the dominant mechanism, respectively. A more recent theoretical study highlighting the importance of both correlations for low temperature ordering[7] represents a potential breakthrough and suggests that a bare description of low temperature VO_2 as purely either a Mott or a Peierls insulator is insufficient. However, the debate is still ongoing.[8–14]

At low temperatures, VO_2 is insulating and monoclinic, with the dimerization of vanadium ions responsible for the localization of the outer-shell vanadium electrons [Fig. 1(a)]. The V-V pairs are characterized by an intradimer atomic separation reduced relative to the interdimer spacing and a tilting relative to the *c*-axis. Heating VO_2 above the 340 K insulator-metal phase transition temperature produces a rapid increase in electrical conductivity that is accompanied by a relaxation of the lattice to a rutile structure [Fig. 1(b)]. In the high temperature lattice, the vanadium dimers are dissociated resulting in a halving of the unit cell and the release of one conduction electron per vanadium ion. Since the phase transition is first-order, driving the system from the insulating to metallic state requires a latent heat, which is associated with changes to both the lattice and electronic entropy.[15]

The observation that the insulator-metal phase change can alternatively be stimulated by an ultrafast optical pulse,[16] coupled with the increased accessibility of ultrafast laser systems and techniques in recent years, has sparked much experimental investigation of the ultrafast photoinduced phase transition in VO_2. Deciphering its mechanism promises to lend vital insight into the nature of the insulating and metallic states. The subpicosecond time scale of the photoinduced transition to the metallic state has been interpreted as an indicator of possible nonthermal behavior,[17–20] since the insulator-metal change can occur faster than the 1 ps hot carrier relaxation time. The phase change rate further scales with pump pulse width to a minimum transition time of 80 fs,[21] which corresponds to approximately one-half period of the 5.85 THz and 6.75 THz phonons that stretch and twist the V-V dimers and map the insulating lattice onto the metallic lattice. The importance of these structural "transition phonons" has also been identified using ultrafast time-resolved terahertz (THz) spectroscopy (or optical-pump/THz-probe) techniques.[18,20] Using ultrabroadband THz pulses, Kübler *et al*. determined that photoexcitation induces a coherent phonon oscillation at 6 THz in addition to electronic excitations,[18] as illustrated in Fig. 1(c). Their observations led them to propose a model in which the removal of an electron from a vanadium dimer leads to a destabilization of the dimer and a local oscillation, where the lattice settles into the metallic state if the optical pump fluence exceeds some critical, temperature-dependent threshold. While the coherent oscillations were observed for only picoseconds,[18,20] time-resolved x-ray diffraction measurements of the photoinduced transition have revealed that unit cell vibration persists for 100 ps,[22,23] indicating that the disappearance of the 6 THz oscillations from the THz spectroscopy measurements is likely a consequence of a loss of coherence rather than a thermalization of the selectively excited lattice oscillations. Furthermore, the nature of correlated-electron physics in VO_2 has spurred investigations of photoinduced phase

transitions in other materials,[24–27] where observations of coherent excitations[24,26,27] indicate that collective motion may not be exclusive to VO_2, but rather a central feature of ultrafast insulator-metal transitions in materials.[28] Finally, an optical-pump/THz-probe investigation revealing enhanced photosusceptibility of a VO_2 film as its base temperature is increased towards the transition temperature confirms the interplay between thermal and optical effects near room temperature.[19] However, the detailed relationship between temperature and optical excitation is an outstanding question, and the actual nature and functional form of the critical optical-pump fluence threshold for phase switching, especially at low temperatures, has not been fully addressed experimentally. Furthermore, despite encouraging results, including an apparent nonthermal phase change stimulated by coincident electron and optical pulses,[29] the distinction between thermal and nonthermal effects can be obscured at the high temperatures typically studied. Most significantly, the primary question regarding the driving force of the phase transition and its relation to the character of the correlated insulating state remains unsolved.

In this paper, we use time-resolved THz spectroscopy (TRTS) to address each of these outstanding questions through the creation of an optical pump fluence versus temperature phase diagram of the ultrafast photoinduced insulator-metal transition. By exploring a broad range of optical pump fluences and extending the phase diagram to low temperatures, we gain valuable insight into the nature of the VO_2 insulator-metal transition. Specific regions in the phase diagram are defined experimentally by the observed changes to the photoinduced THz conductivity dynamics. As an ultrafast, noncontact probe of nanoscale, transient free-carrier conductivity,[30,31] THz spectroscopy is ideal for studying the VO_2 insulator-metal transition.[18–20,32–36] We show for the first time the ultrafast photoinduced insulator-metal transition in VO_2 below 250 K, and our wide temperature range reveals its functional temperature dependence. (We note that Paskhin *et al.*[20] extended their study down to 10 K but did not have sufficient laser pump fluence to drive the phase transition at low temperatures.) The phase diagram provides strong evidence that the photoinduced phase change does not arise simply from laser-heating effects. Rather, the data can be well-described by a novel nonthermal threshold model that relies on a critical density of 6 THz transition phonons to act as a "structural trigger" for the insulator-metal lattice change. Crucially, the transition phonons can be selectively excited by hole photodoping[18,20] to a non-equilibrium population, so the photoinduced transition requires less energy than heating the film across the phase transition temperature. Furthermore, the photoinduced phase transition can be driven over subpicosecond (<0.5 ps), ultrafast time scales but only if a critical electron density equal to the electron density in the fully metallic state is excited. Since the critical 6 THz phonon density represents a threshold for breaking the Peierls distortion and the critical electron density is required to alleviate the on-site repulsion and melt the Mott state, the ultrafast insulator-metal phase transition can be described as a breaking of the cooperative Mott-Peierls insulating state. However, a low temperature region of the phase diagram with unique THz conductivity dynamics reveals the existence of an "intermediate" metallic state formed by breaking the Mott condition while leaving the Peierls distortion intact. Finally, we observe nucleation and growth of metallic nanodomains [Fig. 1(d)] over picoseconds time scales that are consistent with our interpretation of the transient conductivity dynamics described in the phase diagram.

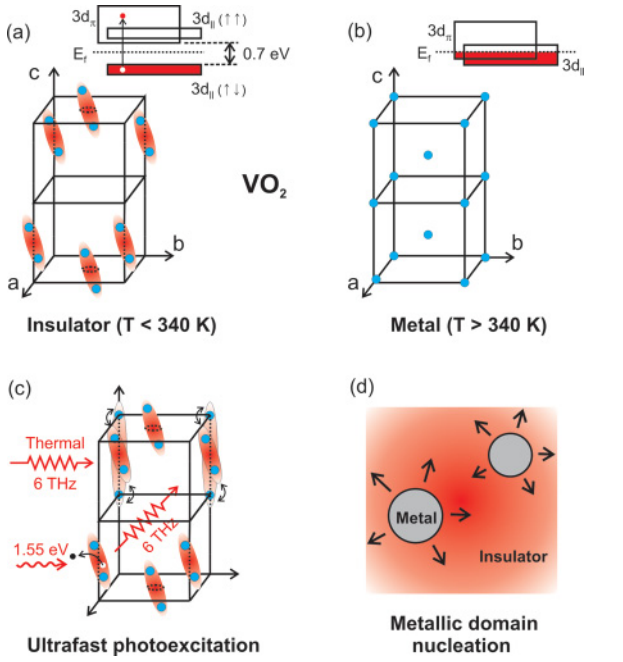

FIG. 1. (Color online) Photoinduced insulator-metal phase transition in VO_2. (a) Low-temperature, monoclinic lattice associated with vanadium dimerization and insulating band structure. (b) High-temperature, rutile lattice with metallic band structure. Orange (gray)-filled regions of the band structure denote occupied states. Only vanadium ions are shown in the lattice structures. In the metallic state, each V is centered in an oxygen octahedron, which remains stationary across the transition. (c) Photoexcitation with 800-nm (1.55 eV) pump pulses results in the excitation of conduction electrons and the selective excitation of 6 THz phonons, which map the insulating lattice onto the metallic lattice. (d) Nucleated metallic nanodomains grow over time if sufficient structural relaxation in the form of a critical density of 6 THz phonons has been achieved in the surrounding region.

II. SAMPLE CHARACTERIZATION AND EXPERIMENTAL DETAILS

Key in our ability to interpret the phase diagram is the detailed, steady-state sample characterization already reported in Ref. 32 where terahertz time-domain spectroscopy (THz-TDS) was used to measure the increase in THz conductivity as the VO_2 film was heated through the insulator-metal transition. As a result, we have a detailed map of the THz conductivity progression in the thermal transition region that provides an essential benchmark for the ultrafast photoinduced THz conductivities reported here. Spectroscopic analysis of the heated transition reported in Ref. 32 not only provides crucial parameters for comparison with the thresholds in the photoinduced transition phase diagram but also allows for a reduction of the number of degrees of freedom in the analysis of the photoinduced transient metallic state detected via time-resolved terahertz spectroscopy.

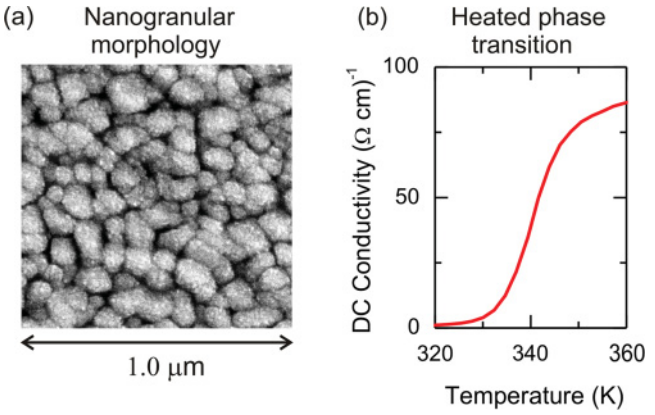

FIG. 2. (Color online) (a) Scanning electron microscope image of the nanogranular VO_2 film. (b) DC conductivity of the film heated through the insulator-metal phase transition measured by four-point probe.

Details of the sample growth and morphology have been discussed elsewhere.[32] Briefly, the 130-nm-thick VO_2 film was deposited by sputtering on a 500-μm-thick a-cut sapphire substrate. The film has nanogranular morphology, as shown in Fig. 2(a), with an average nanograin diameter of 94 nm with a standard deviation of 26 nm. The nanograins themselves are polycrystalline, where the crystallinity was confirmed by x-ray diffraction. The filling fraction of the film was estimated to be about 0.6.[32] It is important to consider potential morphology-based complications that may modify the intrinsic behavior of the VO_2 phase transition. Size-dependent effects have been observed in VO_2 films and nanostructures[37–40] (for example, an unusual, low-temperature insulating lattice structure in VO_2 nanoparticles[38]) but do not appear above a threshold size in the range of 20–50 nm.[38,39] Consequently, we do not expect the nanograin dimensions to play a significant role in the phase transition of our sample. As for the polycrystalline nature of the nanograins themselves, studies of the photoinduced VO_2 phase transition have been largely confined to polycrystalline samples to date. Single crystal VO_2 is available but has the well-known limitation of fracturing upon thermal cycling, making many potential studies unfeasible. While it is generally assumed that polycrystalline samples are an accurate representation of the intrinsic nature of VO_2, some differences have been observed.[41] For example, polycrystalline VO_2 films tend to exhibit larger insulating and smaller metallic conductivities compared to single crystals due to a high density of defect sites. Overall, we believe that our nanogranular thin film sample will provide good physical insight into the insulator-metal phase transition in polycrystalline VO_2, and by extension, into the intrinsic nature of the phase transition in pristine single crystal VO_2. In the analysis of the phase diagram for this sample, the nanogranular-filling fraction will need to be taken into consideration. However, knowledge of the sample morphology gained from the SEM pictures will allow for accurate calculations. It should be noted that a detailed understanding of the effects of sample morphology on carrier transport for ultrafast studies of polycrystalline VO_2 thin films does not appear to be common. Based on the strong influence of nanograin boundary scattering on carrier motion,[32] one must proceed with caution when detecting and interpreting the emergence of the metallic state through free-carrier motion. The well-understood carrier conductivity in the thermally induced metallic state in our sample[32] provides the essential map for the phase diagram.

The thermal transition of the VO_2 film in the heated direction is centered at 340 K, beginning at 330 K and ending at 350 K, as shown in Fig. 2(b). The relatively low dc conductivity compared to some other polycrystalline VO_2 samples is a consequence of the suppression of long-range conductivity by nanograin boundary scattering and is discussed extensively in Ref. 32. Above 350 K, free-carrier absorption in the metallic state resulted in a 33.5% reduction of the transmitted THz pulse peak relative to the transmission in the insulating state (<330 K).[32] The THz conductivity change observed upon heating the nanogranular thin film sample past the transition temperature was described in Ref. 32 using the Drude-Smith model, a modified Drude model[42] capable of reproducing the localization signature caused by nanograin boundary confinement.[30–32,43–47] The average electron density in the fully metallic state was found to be $(5.2 \pm 0.4) \times 10^{20}$ electrons/cm^3.[32]

In the present study, the transient THz conductivity dynamics for a given optical pump fluence and temperature were measured by observing the modulation of the peak of the transmitted THz probe pulse ($-\Delta T/T$) as a function of pump-probe delay time, as illustrated in Fig. 3. An amplified Ti:sapphire laser system was used to produce 100-fs, 800-nm pulses, which were split into optical pump, THz generation, and THz detection beams. The THz pulses were generated by optical rectification in a [110] ZnTe crystal. The amplitude and phase information of THz pulses transmitted through the sample were coherently detected in another [110] ZnTe crystal by free-space electro-optic sampling with the detection beam. The 800-nm pump pulses were collinear with the THz probe pulses and illuminated the sample at normal incidence. A delay stage controlled the delay time between optical pump and THz probe pulses, and the rise time of the pump-induced modulation of the THz probe pulse transmission was limited to 0.5 ps. The sample was mounted on a cold finger behind a 1-mm aperture. The pump beam diameter was set to 2 mm in order to obtain the necessary pump fluences for driving the phase transition at low temperatures. However, the aperture ensured uniform pump beam illumination of the VO_2 film, as confirmed by spectroscopy of a GaAs test sample, and allowed for an accurate calibration of the incident pump fluence. In order to accurately calculate the absorbed pump pulse energy in the film, we measured the reflection (30.5%) and penetration depth (288 nm) of the VO_2 film for our pump wavelength of 800 nm. In finding the penetration depth using a UV-VIS spectrometer, care was taken to properly reference the transmission through the VO_2 because the reflection off the film and the reflection off the bare substrate were significantly different. Furthermore, when converting the absorbed pump-pulse energy density at the back surface of the film into a corresponding incident pump fluence, the contribution of the pump reflected off the VO_2-sapphire interface was included. Both the sample holder and the entire THz beam path were enclosed in a vacuum chamber so the THz pulses were unaffected by water vapor or window absorption.

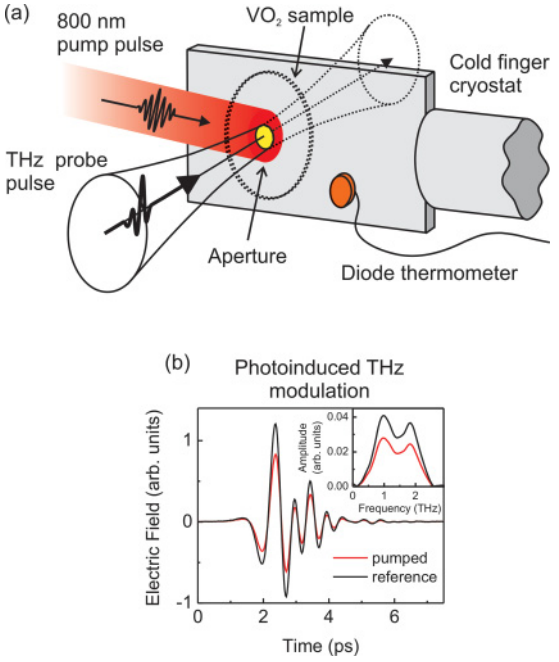

FIG. 3. (Color online) (a) Experimental setup for time-resolved THz spectroscopy of the VO_2 film. The sample is mounted behind an aperture on a cold finger that can be cooled to 17 K. The insulator-metal phase transition is photoinduced in the VO_2 film by an 800-nm, 100-fs optical pump pulse and then probed by a picosecond-duration THz probe pulse. (The 800-nm pump pulse, which is colinear with the THz probe pulse in the experiment, is displaced in the figure for clarity.) (b) The electric field of the transmitted THz probe pulse is modulated by free carrier absorption in the photoinduced metallic state. Reference and pumped waveforms indicate THz probe pulse transmission through the insulating state and photoinduced metallic state, respectively. The inset shows the THz pulse bandwidth.

The cold finger was cooled with liquid helium, and the sample temperature could be set and held constant with a maximum deviation of 0.1 K down to 17 K. At each temperature setpoint the system was given 30 minutes to stabilize to ensure full thermalization of the VO_2 sample.

III. RESULTS AND DISCUSSION

A. Transient THz conductivity dynamics

Using 800-nm, 100-fs pump pulses, the characteristic optical pump-fluence dependence of the transient THz conductivity of the VO_2 film at low [Fig. 4(a), 54.6 K] and high [Fig. 4(b), 288.3 K] temperatures was found to be markedly different. The changes to the THz dynamics for a given pump fluence as a function of temperature are further highlighted in Fig. 4(c) and Fig. 4(d). At high temperatures, the progression of the THz response with increasing pump fluence closely resembled the dynamics reported in previous optical-pump/THz-probe studies of VO_2 above 250 K.[18–20,35] The low-fluence signal is characterized by a sharp, semiconducting-like peak with a 0.5 ps rise time (limited by the setup) and a fast decay time on the order of 1 ps. Other studies have observed similar behavior in VO_2 at low fluences and reported a decay that is faster than exponential, indicative of self-trapping.[18,20] Above a certain optical pump-fluence threshold at high temperatures,

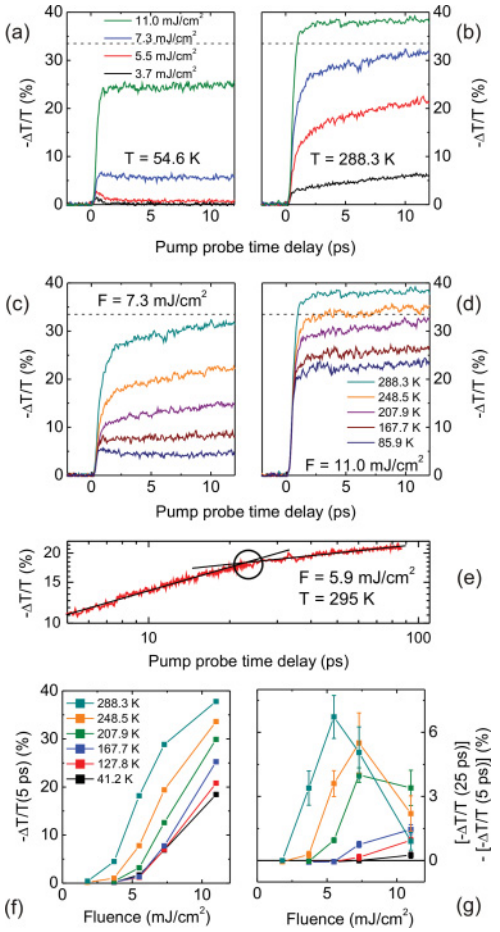

FIG. 4. (Color online) Optical-pump/THz-probe dynamics of the ultrafast photoinduced metallic state in the VO_2 film. The negative differential modulation of the THz pulse transmission, $-\Delta T/T$, represents the photoinduced conductivity dynamics in the VO_2 sample. THz conductivity dynamics at (a) 54.6 K and (b) 288.3 K illustrate the differences in onset and evolution of the metallic state at low and high temperatures, respectively, as a function of optical pump fluence. The THz conductivity dynamics at fluences of (c) 7.3 mJ/cm^2 and (d) 11.0 mJ/cm^2 illustrate the progression of the conductivity response as a function of temperature at constant fluence. The fast initial rise of the THz modulation signal is limited by the 0.5-ps time resolution of the time-resolved THz spectroscopy setup. After 0.5 ps, a slow rise in THz conductivity is observed at high temperatures and fluences. At low temperatures and fluences, an intermediate response emerges with no slow-rise behavior. The horizontal dashed line indicates the THz modulation observed for the fully metallic state at 350 K relative to the low-temperature, insulating state (Ref. 32). (e) Log-log plot of the slow rise THz conductivity dynamics at 295 K and 5.9 mJ/cm^2 showing a crossover between two characteristic time scales at 20 ps following excitation. Black solid lines are guides for the eye. (f) The fluence dependence of the THz pulse-peak modulation at 5 ps pump-probe delay time reveals an increasing pump fluence threshold for the onset of the metallic state with decreasing temperature. (g) The difference between the THz pulse-peak modulation at 25 ps and 5 ps following optical excitation is used to estimate the magnitude of the slow-rise component. Above 180 K, the onset of the slow rise coincides with the metallic onset, but below 180 K the emergence of the slow rise occurs at larger fluences than the metallic threshold, indicative of intermediate metallic-state dynamics with no slow-rise character.

the rapid decay is replaced by a slowly rising, long-lived conductivity commonly associated with the photoinduced metallic state. The slow-rise component contains two distinct time scales lasting 20 ps and 100–200 ps, as shown in Fig. 4(e). Further increasing the fluence eventually leads to a fast, step-function-like THz conductivity response with a THz pulse-peak modulation consistent with steady-state THz measurements of the VO_2 film heated well above the transition temperature.[32] The low temperature dynamics, however, differ significantly in the evolution of the semiconducting peak into the long-lived, slowly rising metallic conductivity. Specifically, an intermediate response exists at low temperatures in which the transient metallic conductivity exhibits no slow rise. The slow-rise behavior emerges only above a second fluence threshold, though suppressed in magnitude relative to the transient behavior observed at high temperatures. Additionally, the optical pump fluences required to initiate the long-lived conductivity and full THz pulse-peak modulation increase with decreasing temperature.

To construct an ultrafast transition phase diagram, the optical pump-fluence thresholds for the onsets of the various observed dynamical phenomena were determined over a wide range of temperatures. The THz modulation signals at pump-probe delay times of 5 ps and 25 ps were selected as representative points for quantifying the long-lived metallic conductivity, and their difference was used to represent the magnitude of the slow rise. Examples of the pump-fluence dependence of the THz probe modulation at 5 ps following photoexcitation at various temperatures are shown in Fig. 4(f), and the corresponding fluence dependence of the slow-rise component is shown in Fig. 4(g). The point at which a THz pulse-peak modulation of 33.5% (observed at 350 K upon heating) was achieved at 5 ps and 25 ps was also determined to indicate the formation of the fully metallic state throughout the film.

B. Phase diagram of the ultrafast photoinduced insulator-metal transition

1. Constructing the phase diagram

The measured fluence-temperature thresholds for the onsets of characteristic THz conductivity dynamics were used to populate the phase diagram of the ultrafast photoinduced insulator-metal transition in the VO_2 sample, as shown in Fig. 5. The two-dimensional set of points divides the fluence-temperature space of the phase diagram [Fig. 5(a)] into four regions with distinct THz conductivity dynamics [Fig. 5(b)]. In region A (dark cyan) the incident fluence is insufficient to induce long-lived conductivity, and only a fast ($\sim$1 ps), small amplitude, semiconductor-like response is observed. Region B (cyan) exists only below 180 K and is populated by fluence-temperature points where the THz dynamics exhibit a long-lived but slowly decaying conductivity. Region C (yellow) is characterized by a transient conductivity that shows the distinctive slow-rise behavior over a 100-ps time scale. Region D denotes full metallic modulation of the THz pulse peak ($-\Delta T/T \geqslant 33.5\%$) within 5 ps and can be represented approximately by a step function with a height corresponding to the full metallic modulation. Examples of photoinduced conductivity transients taken along vertical cuts through the phase diagram at low (80 K) and high (225 K) temperatures are shown for reference in Fig. 5(b).

The phase diagram is highlighted by a number of striking features. First, the lowest fluence threshold below 180 K (at the boundary between regions A and B) is approximately constant. Above 180 K, the lowest fluence threshold (between regions A and C) decreases approximately linearly with increasing temperature. Our metallic fluence thresholds observed at high temperature are lower than typical values reported in the literature[18,20,35] by a factor of approximately 0.6, which is consistent with the filling fraction of 0.6 measured by SEM in our nanogranular film.[32] (The nanogranular structure of the VO_2 film looks homogenous to the incident optical pump pulse, so the absorbed energy we measure is concentrated within the nanograins. We note, however, that the filling fraction of the film does not play a role in the construction of the phase diagram.) Furthermore, the points indicating a completely metallic film (at the boundary between regions C and D) have a clear nonzero fluence intercept at the thermal transition temperature (shaded region), indicating that a latent heat is required to drive the complete phase change.

2. Comparison to thermal predictions for laser-induced heating

The phase diagram cannot be explained by laser-induced heating of the film. Based on a 750 K Debye temperature[48] and a room temperature heat capacity of 3.0 J/cm^3 K,[49,50] and accounting for the 0.6 film-filling factor,[32] the heat capacity of the insulating VO_2 film is known at all temperatures. The latent heat is also known (235 J/cm^3, Ref. 49) and can be similarly corrected using the nanogranular filling fraction (235 J/cm^3 $\times$ 0.6 = 141 J/cm^3). Following Ref. 20, the thermal properties are assumed to be the same for single crystal and polycrystalline VO_2 for the purposes of a laser-heating prediction. Furthermore, our detailed knowledge of the optical penetration depth and the reflectivity of the pump pulse permits us to make an accurate laser-heating estimate for our film and determine the incident fluence needed to deposit a specific energy density at a given film depth. Consequently, the minimum incident fluence thresholds to thermally induce the metallic state by laser heating can be calculated by assuming that all of the *absorbed* pump-pulse energy goes into heating the film. The long-dashed line in Fig. 5(a) corresponds to the incident fluence required to heat the front surface of the VO_2 film to 330 K, the minimum requirement for the possible occurrence of any heated phase change. The short-dashed line in Fig. 5(a) shows the lowest incident fluence that could drive a full thermal phase transition across the entire thickness of the VO_2 film, where the incident pump fluence must be sufficient to raise the average temperature of the whole film to 350 K and overcome the latent heat associated with the heated phase transition to the metallic state. Finally, the dotted line in Fig. 5(a) indicates the incident fluence threshold to heat the back surface of the film to 350 K and supply the latent heat, a more likely estimate for the fluence required to drive the phase transition throughout the whole film via heating.

Near room temperature the laser-heating predictions are close to the measured metallic onset [black triangles and orange squares in Fig. 5(a)] and full transition [filled navy blue diamonds and hollow brown diamonds in Fig. 5(a)] data,

as has been noted in previous studies.[19,20] However, our wide temperature range reveals a drastic divergence of the observed thresholds from thermal predictions at low temperatures, where the long-lived metallic conductivity can be photoinduced by fluences well below what would be necessary to drive the phase transition thermally.[51] Consequently, we rule out laser-induced heating as a mechanism for the observed onsets in THz conductivity dynamics and conclude that the ultrafast photoinduced insulator-metal transition is indeed a nonthermal process.

3. *Nonthermal critical-threshold model*

We propose a nonthermal model based on critical densities of both 6 THz transition phonons and electronic excitations to explain the phase diagram and successfully describe all observed features using only one free parameter. Phonons with frequencies close to 6 THz are believed to be crucial for the structural relaxation of the VO_2 lattice at the insulator-metal transition.[18,20,21] In our model, a critical density of these phonon excitations acts as a "structural trigger" for transforming the monoclinic lattice into the rutile structure associated with the high-temperature metallic state. Once the structural trigger has been achieved, excess energy can contribute directly to the latent heat and drive the phase transition to the fully metallic state via "transition-phonon-triggered" nucleation. Transition-phonon-triggered nucleation generates expanding, fully metallic nanodomains on a 100 picosecond time scale, as confirmed by THz spectroscopy (Sec. III.C), and is reminiscent of the percolative domain formation directly imaged in the heated transition.[52,53] However, metallic domain nucleation can be sped up to subpicosecond (<0.5 ps) time scales if, in addition to the structural trigger, a critical electron density exactly equal to the metallic electron density is also photoexcited by the pump pulse. This ultrafast route to domain formation is referred to here as "photoexcited-electron-assisted" nucleation. In both processes, transition phonons provide a means to undo the low-temperature structural distortion of the correlated insulating phase, and the critical transition phonon density appears to represent a threshold above which the Peierls state can be destroyed. The critical electron density, on the other hand, may be due to a density-driven Mott transition, where a depleted number of carriers allows for transport that circumvents strong on-site repulsion. Therefore, our nonthermal critical-threshold model builds on recent theoretical[7] and experimental[54] results consistent with a description of the phase change as a cooperative Mott-Peierls transition.

We evaluated the incident pump fluence required to excite an electron density at the front surface of the film equal to the steady-state metallic density measured in the heated film ($(5.2 \pm 0.4) \times 10^{20}$ electrons/cm^3)[32] assuming each absorbed pump photon yields one electron. The resulting critical electron density prediction [line 1 in Fig. 5(a)] lies within the error bars of all the metallic onset fluence threshold data points below 180 K and agrees well with the average low-temperature experimental threshold fluence of 5.3 ± 0.2 mJ/cm^2. Therefore, the ultrafast, subpicosecond appearance of the long-lived, metallic conductivity at low temperatures seems to correspond to the achievement of a critical electron density exactly equal to the metallic state electron density.

The critical 6 THz transition phonon density that acts as a trigger for the structural relaxation of the lattice and thereby permits nucleation of the rutile metallic phase can be determined from the insulator-metal transition temperature of the VO_2 film. At 350 K, where the phase change is complete, the base temperature is sufficient to have thermally generated the critical 6 THz phonon density throughout the film as a precursor to the transition. The oscillator occupancy of the phonon mode can be determined using Bose statistics, $\langle n(T)\rangle = 1/(\exp(h\nu_k/k_BT) - 1)$, where ν_k is 6 THz, h is Planck's constant, k_B is Boltzmann's constant, and T is the lattice temperature. At 350 K, there are 0.783 transition phonons per oscillator, which defines the critical transition phonon occupancy that triggers the structural transition. Since 6 THz phonons are preferentially excited upon absorption of a near-IR pump photon,[18,20] the occupancy of the 6 THz mode can be raised to the occupancy value at 350 K while all other modes remain at the lattice temperature. Once the critical transition phonon density is achieved, additional energy can contribute to the latent heat and induce nucleation of metallic nanodomains. The presence of a minimum metallic nucleation size would act to shift the metallic onset to a finite fluence offset above the structural-trigger requirement, resulting in a nonzero fluence intercept at the transition temperature, as has been seen previously.[19,20] As expected, the metallic-onset fluence threshold of our data (<1.1 mJ/cm^2 at the 350 K full transition temperature) is much smaller than the latent heat required for the whole front surface (5.7 mJ/cm^2) because the entire surface of the film need not be switched to observe a modulated THz signal. The transition-phonon-triggered nucleation of nanodomains containing the fully metallic phase acts on a characteristic time scale of 100–200 ps, possibly corresponding to the lifetime of the 6 THz phonons.[22,23] Furthermore, once initiated, the metallic nanodomains can expand outwards because the surrounding insulating regions contain the necessary structural trigger in the form of the critical density of 6 THz phonons. Nanodomain creation and expansion are the sources of the slow-rise THz conductivity dynamics. Finally, the initial appearance of the long-lived, metallic THz conductivity above 180 K is due to transition-phonon-triggered nucleation.

Using the absolute critical phonon density ($\langle n(350\,\mathrm{K})\rangle = 0.783$) and oscillator-occupancy temperature dependence, the 6 THz phonon deficit to be overcome by selective photoexcitation can be calculated and used to simultaneously fit the experimental fluence threshold for the long-lived conductivity above 180 K and the slow-rise onset at all temperatures, $F(T) = F_o(0.783 - \langle n(T)\rangle)$, [line 2 in Fig. 5(a)]. The single free parameter used for the fit is the incident fluence scaling factor, F_o. Converting F_o into an equivalent absorbed energy density at the front surface of the film reveals that the absorbed pump-photon density required to excite one 6 THz phonon per oscillator at 0 K is 10.4×10^{20} photons/cm^3, exactly double the electron density in the fully metallic phase. While it is tempting to pursue the source of this relationship, we are hesitant to ascribe an interpretation without knowing the physical extent of an oscillator.

Interestingly, region B of the phase diagram in Fig. 5(a) is filled with fluence-temperature points that satisfy a special critical-threshold criterion observable only at low

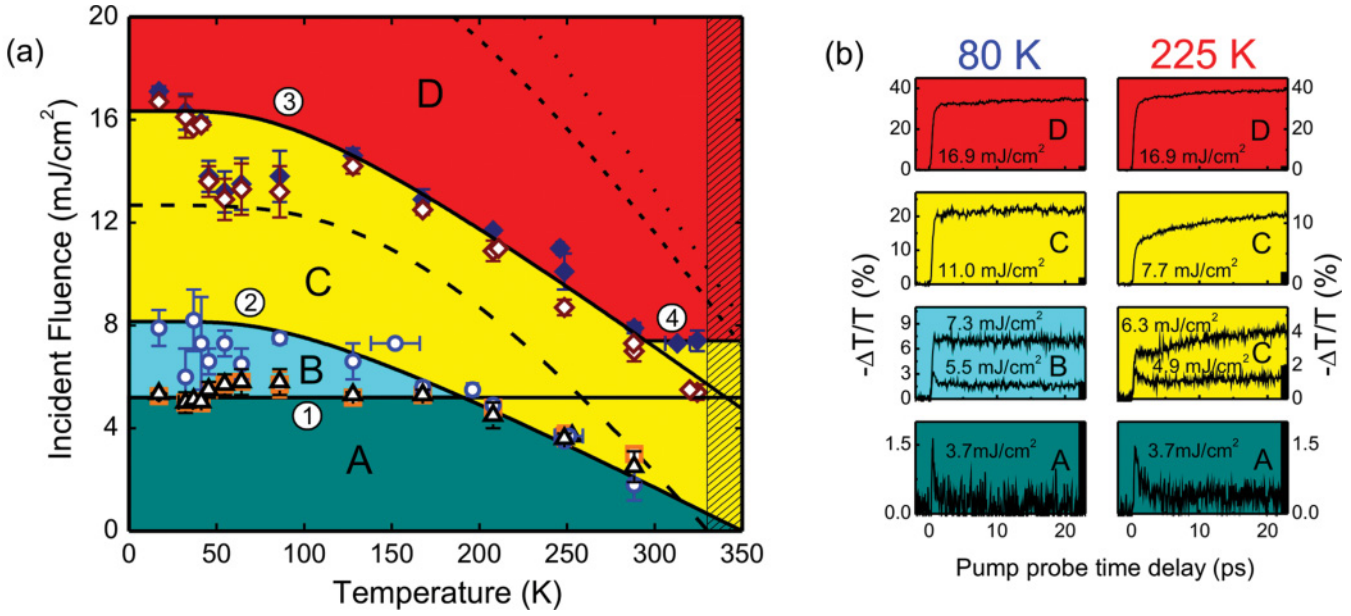

FIG. 5. (Color online) (a) Phase diagram of the ultrafast photoinduced insulator-metal transition of VO_2. Regions A, B, C, and D are defined by their characteristic THz dynamics. Orange squares and black triangles indicate the thresholds for the appearance of the metallic state 5 ps and 25 ps after photoexcitation, respectively. Blue circles indicate thresholds for the onset of slow-rise dynamics. Filled navy blue diamonds denote the achievement of the fully metallic THz pulse modulation ($-\Delta T/T \geqslant 33.5\%$) 5 ps following photoexcitation, while hollow brown diamonds indicate the fully metallic state is formed at 25 ps. Line 1 corresponds to the incident pump fluence needed to excite the metallic electron density at the front surface of the film (see text), while line 2 is the incident fluence required to raise the front surface 6 THz phonon population to the critical density. Line 3 indicates the incident fluence required to excite the critical 6 THz phonon density and supply the latent heat for the structural transition at the back surface of the film. Line 4 denotes the incident fluence required to directly photoexcite the critical electron density at the back surface of the film. As a result, region A represents the insulating state, region B represents the ultrafast photoinduced formation of the intermediate metallic state (Mott melting), region C represents the photoinduced nucleation and growth of the metallic state, and region D represents the ultrafast (<0.5 ps) photoinduced nucleation of the full metallic state throughout the film. The steady-state insulator-metal transition region is denoted by the hatched pattern. The incident fluences required to heat the front surface of the sample to 330 K (the start of the thermal transition), to raise the average temperature of the film to 350 K (including latent heat), and to raise the back surface temperature to 350 K (including latent heat) are indicated by the long-dashed line, short-dashed line, and dotted line, respectively. (b) Examples of THz conductivity dynamics taken along vertical cuts through the phase diagram at 80 K and 225 K.

temperatures. In region B the incident fluence is sufficient to excite the critical electron density at the front surface of the film but insufficient to generate the critical density of 6 THz transition phonons required to trigger the structural transition. The appearance of a metallic conductivity without lattice relaxation is evidence for an intermediate, monoclinic metallic state with a defeated Mott mechanism but an intact Peierls distortion [region B in Fig. 5(a)]. A monoclinic lattice in the absence of on-site repulsion has been shown to behave as a metal,[7] and the formation of a metallic band structure prior to the full structural transition has been suggested as an intermediate step in the ultrafast phase transition.[55–57] The observed THz conductivity dynamics in region B provide further support for the existence of an intermediate metallic state. Since the insulating lattice surrounding the nucleated, intermediate metallic state does not contain the structural trigger, any domains formed cannot expand, nor can fully metallic domains be created by transition-phonon-triggered nucleation. Consequently, no slow-rise component in the transient THz conductivity is observed in region B. Therefore, within the framework of our dual threshold model, the unique flat but long-lived THz conductivity transient observed at low temperatures is indicative of a new intermediate metallic state. We acknowledge that an unusual insulating lattice structure has been seen in VO_2 nanostructures at low temperatures that could conceivably be responsible for the distinct THz dynamics, but we do not anticipate that our sample will exhibit such effects based on the sample nanograin sizes.[38]

The onset thresholds of the phase diagram can be summarized as follows. If only the critical electron density is present, the intermediate metallic state, which has the same electron density as the fully metallic phase but not the rutile lattice structure, will be nucleated on subpicosecond time scales. The measured THz conductivity response exhibits an ultrafast, subpicosecond (<0.5 ps) rise to a flat, long-lived transient, as is observed for fluence-temperature points in Fig. 5(a) between lines 1 and 2 below 180 K (within region B). If only the critical 6 THz transition phonon density is present, nanodomains containing the fully metallic phase will be created by transition-phonon-triggered nucleation on a 100 ps time scale. These nanodomains can also expand. The THz conductivity will display a slow rise over 100 ps with no initial subpicosecond step (though the signal at early times may be convoluted with a semiconducting peak that decays away within picoseconds), as is observed for points between lines 1 and 2 above 180 K in Fig. 5(a). Finally, if both critical densities

are present, the phase transition to the fully metallic state will occur via *both* transition-phonon-triggered nucleation over the 100 ps time scale and via photoexcited-electron-assisted nucleation in less than a picosecond. In other words, the rate of the monoclinic-rutile lattice change triggered by the critical density of transition phonons is limited in the absence of the critical electron density. However, direct photoexcitation of the critical electron density in addition to the structural trigger appears to significantly enhance the speed of the monoclinic-rutile lattice transition. The THz response when both critical densities are present is characterized by an ultrafast step followed by a slow rise to even larger conductivities over 100 ps. This behavior is observed for points on the phase diagram in Fig. 5(a) above line 1 (in region C) for temperatures larger than 180 K and above line 2 (in region C) for temperatures less than 180 K.

Where the experimental onsets for characteristic THz dynamics reveal information about the initial formation of the metallic state, the full THz pulse-peak modulation data provides insight into the requirements for the complete phase change in the film. To observe the 33.5% THz peak reduction measured in the high-temperature, fully metallic state, the entire film must be driven across the phase transition. Inducing the insulator-metal change of a complete layer, specifically the back surface of the film, rather than just nucleating metallic nanodomains, necessitates the latent heat be provided in addition to the structural trigger. Furthermore, to ensure the full film undergoes the phase transition on the ultrafast, subpicosecond time scale, the critical electron density must be directly photoexcited at the back surface. Since the absorbed pump energy is deposited by photoexciting dimer electrons, this condition will be satisfied as long as the incident pump fluence exceeds 7.4 mJ/cm^2. This threshold is denoted by line 4 in Fig. 5(a) and corresponds to an absorbed photon density at the back surface of the film equal to the critical electron density. The optical pump fluence required to raise the 6 THz phonon occupancy to the critical transition phonon density at the back surface of the film is similarly found by converting the fluence scaling factor for the front surface, F_o, into a back surface scaling factor, F_1, using the optical reflectivity and penetration depth (and considering the reflection from the VO_2-sapphire interface), as discussed in Sec. II. Otherwise, the formula describing the incident fluence required to produce the critical transition phonon density at the back surface of the film is identical to the relation used to obtain line 2 in Fig. 5(a). Finally, the latent heat that drives the monoclinic-rutile lattice change must be added to the structural-trigger excitation energy for a full-film transition. Though the details are not entirely clear, the latent heat for the photoinduced transition appears to be the latent heat for the heated transition (141 J/cm^3) minus the energy needed to excite the critical electron density across the 0.7 eV bandgap (58 J/cm^3). The resulting energy density (83 J/cm^3) might be interpreted as the structural component of the latent heat. An incident fluence of 4.75 mJ/cm^2 is needed to deposit 83 J/cm^3 at the back surface of the film, so the total incident fluence required to drive the ultrafast, subpicosecond transition of the entire film to the fully metallic state is 4.75 mJ/cm^2 + $F_1(0.783 - \langle n(T)\rangle)$. The resulting prediction [line 3 in Fig. 5(a)] agrees well with the measured fluences (below 298 K) needed to achieve the THz pulse-peak modulation characteristic of the fully metallic state.

As expected, the fluence needed to nucleate the fully metallic state throughout the film within a subpicosecond time scale, which is experimentally defined by a THz modulation of 33.5% 5 ps following photoexcitation [filled navy blue diamonds in Fig. 5(a)], saturates where line 3 meets line 4 in Fig. 5(a). Since the slow-rise component contributes negligibly to the THz conductivity within the first 5 ps, the entire insulator-metal phase change must occur in the initial fast-step component via photoexcited-electron-assisted nucleation, which is only possible if the critical electron density is directly photoexcited. Conversely, observations of the 33.5% THz modulation 25 ps following photoexcitation [hollow brown diamonds in Fig. 5(a)] continue to follow line 3 because transition-phonon-triggered nucleation contributes significantly to the THz conductivity. It is perhaps surprising that, based on the 350 K fluence intercept of line 3 in Fig. 5(a), the structural component of the latent heat seems to be the only part necessary for the photoinduced phase transition. It is possible that the latent heat of our film is somehow reduced by the nanogranular film morphology to 83 J/cm^3, though we note that the value of the latent heat can neither account for the divergence of thermal predictions, nor affect the physical picture outlined in the critical-threshold model.

C. Time-resolved terahertz spectroscopy of metallic domain growth

To explore the slow-rise THz dynamics and confirm our interpretation of the phase diagram data, we extracted the complex THz conductivity of the photoinduced signal as a function of pump-probe time delay. We mapped the time dependence of the conductivity for multiple pump fluences at room temperature. Examples of the THz conductivity observed at pump-probe delay times of 5 ps, 20 ps, and 200 ps are displayed in Fig. 6(a). As expected, the conductivity signature of the photoexcited film is similar to that observed in steady-state THz experiments for the film heated into the metallic state.[32] A real conductivity (σ_1) that increases with frequency coupled with a negative imaginary conductivity (σ_2) in the THz regime is characteristic of mesoscopically localized charge carriers in materials.[32,43–47] The localization-suppressed THz conductivity of our nanogranular film heated into the metallic state was well-described by the Drude-Smith model, a modified Drude model which includes a correction to account for localization due to structural confinement, as is discussed extensively elsewhere.[32,42–44] The Drude-Smith conductivity formula is given by

$$\tilde{\sigma}(\omega) = \frac{ne^2\tau_{DS}}{m^*}\left(\frac{1}{1 - i\omega\tau_{DS}}\right)\left(1 + \frac{c}{1 - i\omega\tau_{DS}}\right), \quad (1)$$

where, in addition to the conventional Drude parameters n, the macroscopic electron density, and m^*, the carrier effective mass, the Drude-Smith formula contains two parameters associated with carrier localization: τ_{DS} is a modified scattering time that includes effects from both intrinsic-impurity scattering and boundary scattering, while the c-parameter is determined by a combination of the barrier reflectivity and the ratio between the nanodomain diameter and the carrier mean

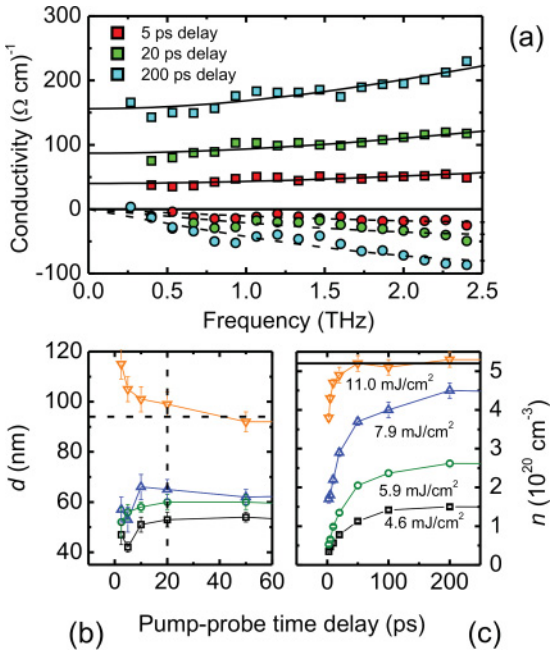

FIG. 6. (Color online) Time-resolved terahertz spectroscopy of metallic nanodomain formation and expansion. (a) Examples of the real (squares) and imaginary (circles) photoinduced THz conductivity at 295 K for an incident fluence of 5.9 mJ/cm^2 at various pump-probe delay times. Solid line are fits to the Drude-Smith model. (b) Pump-probe delay time dependence of the effective metallic nanodomain size, d, and (c) macroscopic electron density, n, extracted from the Drude-Smith fits at various pump fluences at 295 K. The average nanograin size in the film (94 nm) is denoted by a horizontal dashed line in (b) and the vertical dashed line marks a pump-probe delay time of 20 ps. Since the electron density is an average value for the film, a density less than the full metallic density [solid horizontal line in (c)] indicates that only a fraction of the film has undergone the transition to the metallic state.

free path. For full localization and a zero dc conductivity, $c = -1$, while for $c = 0$ Drude behavior is recovered. For our VO_2 sample, it was shown in Ref. 32 that τ_{DS} and c could effectively be re-parameterized in terms of the Fermi velocity v_F, the metallic nanodomain diameter d, and bulk scattering time τ, such that $\tau_{DS} = d\tau/(d + v_F\tau)$ and $c = -1/(1 + d/20v_F\tau)$.[32,43,44]

Analysis of the heated transition further revealed the identity of the Fermi velocity (4.3×10^5 m/s) and the bulk scattering time (an approximately constant value of 22 fs throughout the heated transition) for our VO_2 film.[32] As a result, the re-parameterization reduces the number of free Drude-Smith fitting parameters to just n and d since the effective mass is assumed to be a constant $m^* = 2m_e$, as was done in Ref. 33. Since d is the effective domain size of a metallic region with 100% carrier reflecting boundaries, if the insulator-metal boundaries in the photoinduced metallic domains do not perfectly repel the incident conduction electrons (as do the nanogranular boundaries, to a good approximation), then d will be an underestimate of the diameter. However, the maximum metallic domain size in the fully metallic film is limited by the nanograin dimensions that have an average diameter of 94 nm.

The re-parameterized Drude-Smith model provides good fits to the THz conductivity at all pump fluences and pump-probe time delays (TRTS was also performed at other temperatures and the Drude-Smith model was consistently accurate). Examples of Drude-Smith fits to the measured THz conductivities are shown in Fig. 6(a). At room temperature, the complex THz conductivity was resolved at multiple positions along the slow-rise curve, and the domain size d and average electron density n were extracted for each spectrum, as plotted in Fig. 6(b) and Fig. 6(c), respectively.

The time dependence of the average electron density of the VO_2 film shows the two possible nucleation processes within region C of the phase diagram [Fig. 5(a)]. Photoexcited-electron-assisted nucleation is likely responsible for the initial nonzero electron densities and finite metallic domain sizes at early times, as it produces the metallic state on subpicosecond time scales (<0.5 ps). Transition-phonon-triggered nucleation, on the other hand, is responsible for the 100–200 ps time scale observed in the slow-rise THz dynamics. A similar nucleation time scale has been seen in Peierls distorted antimony.[58] A possible explanation for the 100-ps time scale in VO_2 is found in studies probing the photoinduced transition using ultrafast x-rays, wherein photoinduced lattice vibrations were shown to persist for 100 ps.[22,23] Thus, within our critical-threshold model, the 100-ps duration of the slow-rise THz dynamics can be interpreted as the lifetime of the photoexcited 6 THz phonons before thermalization occurs. After 100 ps, the transition phonons thermalize, their population decreases below the critical density, and further nucleation of metallic nanodomains cannot occur. Additionally, at high pump fluences, n quickly saturates at the identical electron density measured for the high temperature film [solid line in Fig. 6(c)] when the entire film is turned metallic, supporting the assumption that the metallic states formed by steady-state heating and photoinduced by intense optical pumping are indeed the same.

The magnitude and dynamics of the average nucleated metallic domain size reveal insight into the formation and growth of the photoinduced metallic state in region C of the phase diagram. While the most likely direction for domain expansion is into the film, the initiation of the metallic state at small nucleation sites means that the expansion occurs in three dimensions and therefore displays a decrease in the effective carrier confinement, as detected in the THz conductivity spectra. The metallic domains created by fluences in region C are smaller than the average nanograin diameter, 94 nm, indicating enhanced localization and dimensions that do not encompass an entire nanograin. The average metallic domain size exhibits growth in the first 20 ps following excitation, as illustrated in Fig. 1(d), then a saturation and decay. While Bruggeman effective medium theory was shown in Ref. 32 to be inappropriate for our nanogranular sample, it has been used to successfully model a similar metallic domain expansion in VO_2.[19] The high fluence data does not display the same domain expansion since it lies well within region D, where the entire film is driven into the fully metallic state on subpicosecond time scales. A possible explanation for effective domain sizes that exceed the average nanograin diameter at early times is that the excess energy provided to carriers is sufficient to increase their probability of penetrating the nanograin

boundaries. Over time, the boundary reflectivity increases and the effective domain size decays to the 94-nm average nanograin diameter. The short-lived relaxation of carrier confinement explains why a THz pulse-peak modulation in excess of 33.5% can occur for high pump fluences. However, the electron density extracted from the Drude-Smith fits is *never* found to be higher than the metallic electron density measured in the high temperature, fully metallic phase of the film, as shown in Fig. 6(c).

Interestingly, the 20-ps time scale for the growth of the metallic nanodomains appears to correspond to the ballistic spread of 6 THz phonons. An estimate for the time scale of the metallic domain expansion can be made based on the speed of 6 THz phonon propagation through the lattice. The speed of sound in VO_2 is 6.9 nm/ps,[59] so the time for a phonon to travel ballistically from the front to the back of the film is 18.8 ps, which is very close to the 20 ps rise time observed in the THz dynamics, as shown in Fig. 4(e) and Fig. 6(b). The relation of the speed of sound to the slow rise time scale in VO_2 has been similarly identified elsewhere,[35] as has the significance of a shockwave for the propagation of the structural transition.[60]

IV. CONCLUSIONS

In conclusion, we have used time-resolved THz spectroscopy to create a phase diagram for the ultrafast photoinduced insulator-metal phase transition in vanadium dioxide. The phase diagram reveals that the ultrafast photoinduced phase transition is a nonthermal process that requires both a critical density of electronic excitations to melt the Mott state and a critical density of phonon excitations to provide a structural trigger to quench the Peierls state. The structural trigger is defined in terms of a critical density of 6 THz transition phonons that connect the insulating and metallic lattices. Since both the transition phonons and electronic excitations are necessary to drive the ultrafast phase change throughout the film, the full ultrafast insulator-metal transition in vanadium dioxide cannot be viewed as simply either a Mott or Peierls type. However, evidence for an intermediate metallic state is found at low temperatures wherein the Mott state is melted by the achievement of a critical density of electronic excitations, but the Peierls distortion remains intact because of an insufficient density of transition phonons, providing valuable insight into the nature of the insulator-metal phase transition in vanadium dioxide. Expansion of nucleated metallic nanodomains over picosecond time scales is also observed.

ACKNOWLEDGMENTS

This work was financially supported by the Natural Sciences and Engineering Research Council of Canada (NSERC), the Canada Research Chair Program, and the Alberta Informatics Circle of Research Excellence (iCORE). We are grateful for technical support from G. Popowich and D. Mullin and fruitful discussions with F. Marsiglio.

*tcocker@gmail.com
†hegmann@ualberta.ca

[1] F. J. Morin, Phys. Rev. Lett. **3**, 34 (1959).
[2] J. B. Goodenough, J. Sol. Stat. Chem. **3**, 490 (1971).
[3] R. M. Wentzcovitch, W. W. Schulz, and P. B. Allen, Phys. Rev. Lett. **72**, 3389 (1994).
[4] V. Eyert, Ann. Phys. (Leipzig) **11**, 650 (2002).
[5] A. Zylbersztejn and N. F. Mott, Phys. Rev. B **11**, 4383 (1975).
[6] D. Paquet and P. Leroux-Hugon, Phys. Rev. B **22**, 5284 (1980).
[7] S. Biermann, A. Poteryaev, A. I. Lichtenstein, and A. Georges, Phys. Rev. Lett. **94**, 026404 (2005).
[8] M. S. Laad, L. Craco, and E. Müller-Hartmann, Phys. Rev. B **73**, 195120 (2006).
[9] V. S. Vikhnin, S. Lysenko, A. Rua, F. Fernandez, and H. Liu, Solid State Commun. **137**, 615 (2006).
[10] S. M. Woodley, Chem. Phys. Lett. **453**, 167 (2008).
[11] J. M. Tomczak and S. Biermann, Phys. Rev. B **80**, 085117 (2009).
[12] B. Lazarovits, K. Kim, K. Haule, and G. Kotliar, Phys. Rev. B **81**, 115117 (2010).
[13] L. Whittaker, C. J. Patridge, and S. Banerjee, J. Phys. Chem. Lett. **2**, 745 (2011).
[14] V. Eyert, Phys. Rev. Lett. **107**, 016401 (2011).
[15] D. Maurer, A. Leue, R. Heichele, and V. Müller, Phys. Rev. B **60**, 13249 (1999).
[16] M. F. Becker, A. B. Buckman, R. M. Walser, T. Lépine, P. Georges, and A. Brun, Appl. Phys. Lett. **65**, 1507 (1994).
[17] A. Cavalleri, Cs. Tóth, C. W. Siders, J. A. Squier, F. Ráksi, P. Forget, and J. C. Kieffer, Phys. Rev. Lett. **87**, 237401 (2001).
[18] C. Kübler, H. Ehrke, R. Huber, R. Lopez, A. Halabica, R. F. Haglund Jr., and A. Leitenstorfer, Phys. Rev. Lett. **99**, 116401 (2007).
[19] D. J. Hilton, R. P. Prasankumar, S. Fourmaux, A. Cavalleri, D. Brassard, M. A. El Khakani, J. C. Kieffer, A. J. Taylor, and R. D. Averitt, Phys. Rev. Lett. **99**, 226401 (2007).
[20] A. Pashkin, C. Kübler, H. Ehrke, R. Lopez, A. Halabica, R. F. Haglund Jr., R. Huber, and A. Leitenstorfer, Phys. Rev. B **83**, 195120 (2011).
[21] A. Cavalleri, Th. Dekorsy, H. H. W. Chong, J. C. Kieffer, and R. W. Schoenlein, Phys. Rev. B **70**, 161102(R) (2004).
[22] M. Hada, K. Okimura, and J. Matsuo, Phys. Rev. B **82**, 153401 (2010).
[23] M. Hada, K. Okimura, and J. Matsuo, Appl. Phys. Lett. **99**, 051903 (2011).
[24] D. Polli, M. Rini, S. Wall, R. W. Schoenlein, Y. Tomioka, Y. Tokura, G. Cerullo, and A. Cavalleri, Nat. Mater. **6**, 643 (2007).
[25] M. K. Liu, B. Pardo, J. Zhang, M. M. Qazilbash, S. J. Yun, Z. Fei, J.-H. Shin, H.-T. Kim, D. N. Basov, and R. D. Averitt, Phys. Rev. Lett. **107**, 066403 (2011).
[26] H. Okamoto, K. Ikegami, T. Wakabayashi, Y. Ishige, J. Togo, H. Kishida, and H. Matsuzaki, Phys. Rev. Lett. **96**, 037405 (2006).
[27] L. Perfetti, P. A. Loukakos, M. Lisowski, U. Bovensiepen, M. Wolf, H. Berger, S. Biermann, and A. Georges, New J. Phys. **10**, 053019 (2008).
[28] K. Yonemitsu and K. Nasu, J. Phys. Soc. Jpn. **75**, 011008 (2006).
[29] M. S. Grinolds, V. A. Lobastov, J. Weissenrieder, and A. H. Zewail, Proc. Natl. Acad. Sci. **103**, 18427 (2006).

[30]P. U. Jepsen, D. G. Cooke, and M. Koch, Laser & Photon. Rev. **5**, 124 (2011).
[31]R. Ulbricht, E. Hendry, J. Shan, T. F. Heinz, and M. Bonn Rev. Mod. Phys. **83**, 543 (2011).
[32]T. L. Cocker, L. V. Titova, S. Fourmaux, H.-C. Bandulet, D. Brassard, J.-C. Kieffer, M. A. El Khakani, and F. A. Hegmann, Appl. Phys. Lett. **97**, 221905 (2010).
[33]P. U. Jepsen, B. M. Fischer, A. Thoman, H. Helm, J. Y. Suh, R. Lopez, and R. F. Haglund Jr., Phys. Rev. B **74**, 205103 (2006).
[34]H. Zhan, V. Astley, M. Hvasta, J. A. Deibel, D. M. Mittleman, and Y.-S. Lim, Appl. Phys. Lett. **91**, 162110 (2007).
[35]M. Nakajima, N. Takubo, Z. Hiroi, Y. Ueda, and T. Suemoto, Appl. Phys. Lett. **92**, 011907 (2008).
[36]P. Mandal, A. Speck, C. Ko, and S. Ramanathan, Opt. Lett. **36**, 1927 (2011).
[37]R. Lopez, T. E. Haynes, L. A. Boatner, L. C. Feldman, and R. F. Haglund Jr., Phys. Rev. B **65**, 224113 (2002).
[38]Y. Ishiwata, S. Suehiro, M. Hagihala, X. G. Zheng, T. Kawae, O. Morimoto, and Y. Tezuka, Phys. Rev. B **82**, 115404 (2010).
[39]S. Lysenko, V. Vikhnin, A. Rúa, F. Fernández, and H. Liu, Phys. Rev. B **82**, 205425 (2010).
[40]J. Ma, G. Xu, L. Miao, M. Tazawa, and S. Tanemura, Jpn. J. Appl. Phys. **50**, 020215 (2011).
[41]M. Rini, Z. Hao, R. W. Schoenlein, C. Giannetti, F. Parmigiani, S. Fourmaux, J. C. Kieffer, A. Fujimori, M. Onoda, S. Wall, and A. Cavalleri, Appl. Phys. Lett. **92**, 181904 (2008).
[42]N. V. Smith, Phys. Rev. B **64**, 155106 (2001).
[43]L. V. Titova, T. L. Cocker, D. G. Cooke, X. Wang, A. Meldrum, and F. A. Hegmann, Phys. Rev. B **83**, 085403 (2011).
[44]H. Němec, P. Kužel, and V. Sundström, Phys. Rev. B **79**, 115309 (2009).
[45]J. B. Baxter and C. A. Schmuttenmaer, J. Phys. Chem. B **110**, 25229 (2006).
[46]M. Walther, D. G. Cooke, C. Sherstan, M. Hajar, M. R. Freeman, and F. A. Hegmann, Phys. Rev. B **76**, 125408 (2007).
[47]H. Ahn, Y.-P. Ku, Y.-C. Wang, C.-H. Chuang, S. Gwo, and C.-L. Pan, Appl. Phys. Lett. **91**, 163105 (2007).
[48]G. V. Chandrashekhar, H. L. C. Barros, and J. M. Honig, Mater. Res. Bull. **8**, 369 (1973).
[49]C. N. Berglund and H. J. Guggenheim, Phys. Rev. **185**, 1022 (1969).
[50]G. Stefanovich, A. Pergament, and D. Stefanovich, J. Phys.: Condens. Matter **12**, 8837 (2000).
[51]Preliminary measurements for fluence/temperature phase diagrams at pump-excitation wavelengths of 400 nm and 267 nm also exhibit an ultrafast photoinduced phase transition that cannot be explained by laser-induced heating.
[52]M. M. Qazilbash, M. Brehm, B.-G. Chae, P.-C. Ho, G. O. Andreev, B.-J. Kim, S. J. Yun, A. V. Balatsky, M. B. Maple, F. Keilmann, H.-T. Kim, and D. N. Basov, Science **318**, 1750 (2007).
[53]M. M. Qazilbash, A. Tripathi, A. A. Schafgans, B.-J. Kim, H.-T. Kim, Z. Cai, M. V. Holt, J. M. Maser, F. Keilmann, O. G. Shpyrko, and D. N. Basov, Phys. Rev. B **83**, 165108 (2011).
[54]M. W. Haverkort, Z. Hu, A. Tanaka, W. Reichelt, S. V. Streltsov, M. A. Korotin, V. I. Anisimov, H. H. Hsieh, H.-J. Lin, C. T. Chen, D. I. Khomskii, and L. H. Tjeng, Phys. Rev. Lett. **95**, 196404 (2005).
[55]A. Cavalleri, M. Rini, H. H. W. Chong, S. Fourmaux, T. E. Glover, P. A. Heimann, J. C. Kieffer, and R. W. Schoenlein, Phys. Rev. Lett. **95**, 067405 (2005).
[56]T. Yao, X. Zhang, Z. Sun, S. Liu, Y. Huang, Y. Xie, C. Wu, X. Yuan, W. Zhang, Z. Wu, G. Pan, F. Hu, L. Wu, Q. Liu, and S. Wei, Phys. Rev. Lett. **105**, 226405 (2010).
[57]H.-T. Kim, Y. W. Lee, B.-J. Kim, B.-G. Chae, S. J. Yun, K.-Y. Kang, K.-J. Han, K.-J. Yee, and Y.-S. Lim, Phys. Rev. Lett. **97**, 266401 (2006).
[58]D. Fausti, O. V. Misochko, and P. H. M. van Loosdrecht, Phys. Rev. B **80**, 161207(R) (2009).
[59]D.-W. Oh, C. Ko, S. Ramanathan, and D. G. Cahill, Appl. Phys. Lett. **96**, 151906 (2010).
[60]P. Baum, D.-S. Yang, and A. H. Zewail, Science **318**, 788 (2007).